Improved spatiotemporal resolution of anti-scattering super-resolution label-free microscopy via synthetic wave 3D metalens imaging

Yuting Xiao[1,2,4†], Lianwei Chen[1,2,3,4†], Mingbo Pu[1,2,3,4*], Mingfeng Xu[1,2,3,4], Qi Zhang[1,2,3,4], Yinghui Guo[1,2,3,4], Tianqu Chen[1,2,4] and Xiangang Luo[1,2,4*]

[1]National Key Laboratory of Optical Field Manipulation Science and Technology, Chinese Academy of Sciences, Chengdu 610209, China; [2]State Key Laboratory of Optical Technologies on Nano-Fabrication and Micro-Engineering, Institute of Optics and Electronics, Chinese Academy of Sciences, Chengdu 610209, China; [3]Research Center on Vector Optical Fields, Institute of Optics and Electronics, Chinese Academy of Sciences, Chengdu 610209, China; [4]School of Optoelectronics, University of Chinese Academy of Sciences, Beijing 100049, China.
†These authors contributed equally to this work.
*Correspondence: MB Pu, E-mail: pmb@ioe.ac.cn; XG Luo, E-mail: lxg@ioe.ac.cn

This file includes:

Supplementary information for this paper is available at https://doi.org/10.29026/oes.2023.230037

Section 1: Theoretical analysis

The synthetic wave source consists of dual beams generated from two sources: Fig. S1(a) a narrow linewidth continuous laser operating at 1064 nm and Fig. S1(b) a narrow linewidth continuous laser operating at 1064.1 nm. Figure S1(c) explains the concept of the synthetic wave. The single-beam spectrum obtained from the source is shown on the right in which only one spectral channel was used. One of the optical frequencies is 2.8195×10^{14} Hz, and the other optical frequency is 2.8193×10^{14} Hz. Optical frequencies are far too fast to measure in a manner that has become routine for radio frequencies. The frequency difference between the two optical waves is 2.6497×10^{10} Hz. This difference in frequency of a factor of 10^4 led to a link between radio frequency electronics and optics, thus allowing us to enlarge harmonics period from f^{-1} (femtoseconds) to Δf^{-1} (picosecond). Indeed, optically generated microwaves with synthetic waves leverage the ultrahigh optical quality factors and narrow-linewidth lasers mentioned above. Figure S1(d) shows its implementation that rapidly reconstructs the phase. In the process of phase demodulation, the phase can be calculated by measuring the intensity variation of the interference electric field over one synthetic wave period starting from the initial time 0. In our method, the phase shift between the two interference fields will change with time. Thus, we can obtain four intensity
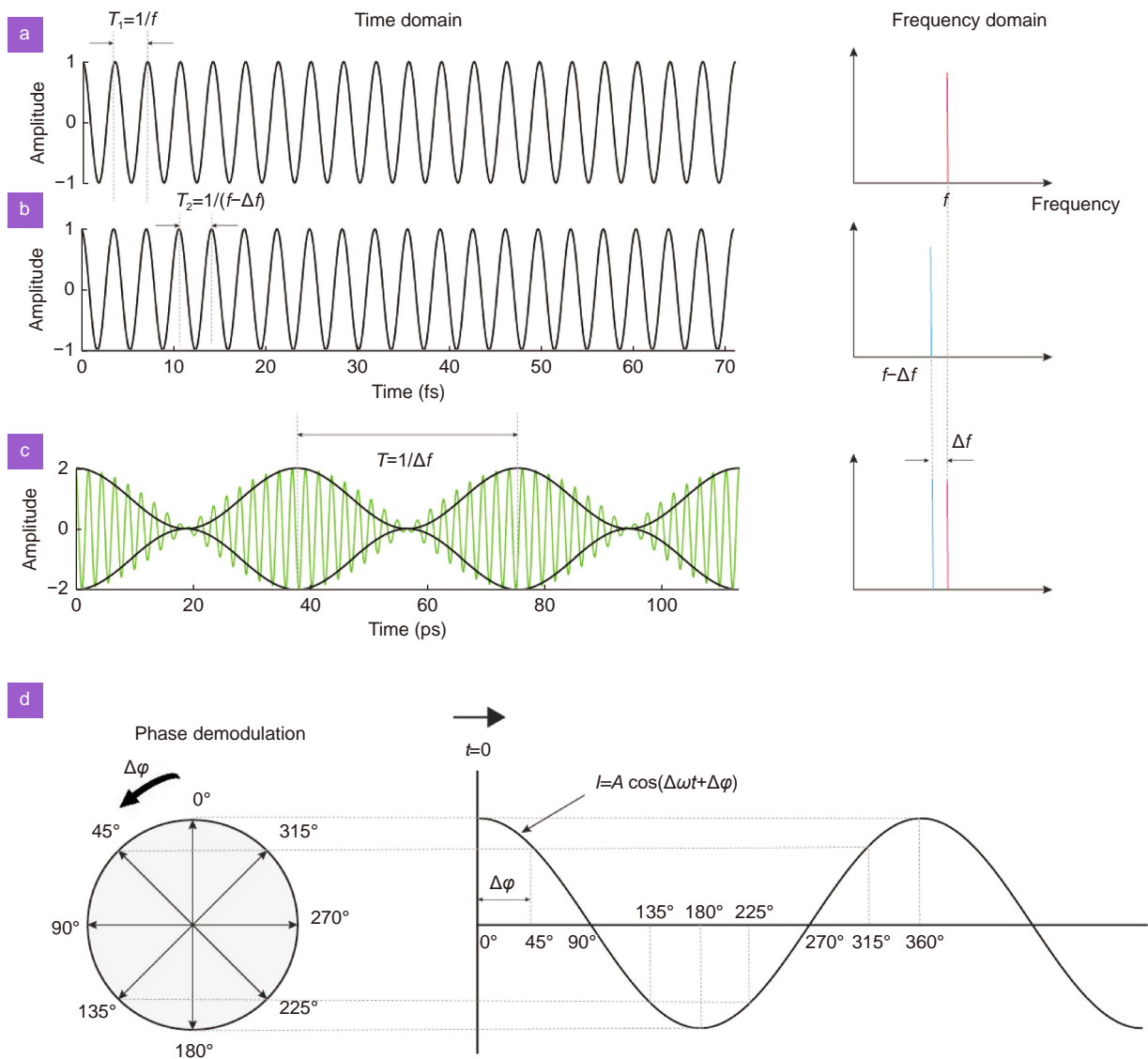

Fig. S1 | Time- and frequency-domain representations of the synthetic waves. (**a**) The continuous optical wave with frequency f and period T_1 is represented as a single tone in the frequency domain. (**b**) The continuous optical wave with frequency $(f-\Delta f)$ and period T_2 is represented as a single tone in the frequency domain. (**c**) The synthetic wave with an envelope period of T is represented as two tones in the frequency domain. (**d**) Illustration of phase demodulation.

values within the dwell time of each pixel for the image acquisition. LS-GLIM needs the liquid crystal to modulate the phase shift four times. Hence, our method is more than four times faster compared to LS-GLIM. Phase demodulation is crucial in many applications, such as optical interference measurements, radar, and communication systems, where it is used to measure or transmit phase information. It allows us to extract useful phase information from complex interference signals, enabling more accurate measurements and communications.

Section 2: Phase reconstruction algorithm

As shown in Fig. S2(a), the beam from the synthetic wave source generation module is focused on the sample plane, and the scattered signal is recorded by the Photomultiplier Tube (PMT). Point scanning technology includes mechanical scanning and beam scanning, among others. At each location, light intensity information are recorded, and then the scanning device moves to the next location. This process is repeated until the entire area has been scanned. As shown in Fig. S2(b), the PMT records the intensity variation curve after scanning the entire image. We perform post-processing based on the scanning module speed. Given an image case that the scanning module speed is 1 pixel/μs: First, we extract intensity information at 1 μs intervals as initial intensity. Next, we extract intensity information for one quarter of the synthetic wave cycle within each 1 μs time interval, starting from the initial time. The four-step phase-shifting method only requires four intensity pieces of information. As shown in Fig. S2(c), phase information is obtained by calculating the intensity information of these four points.
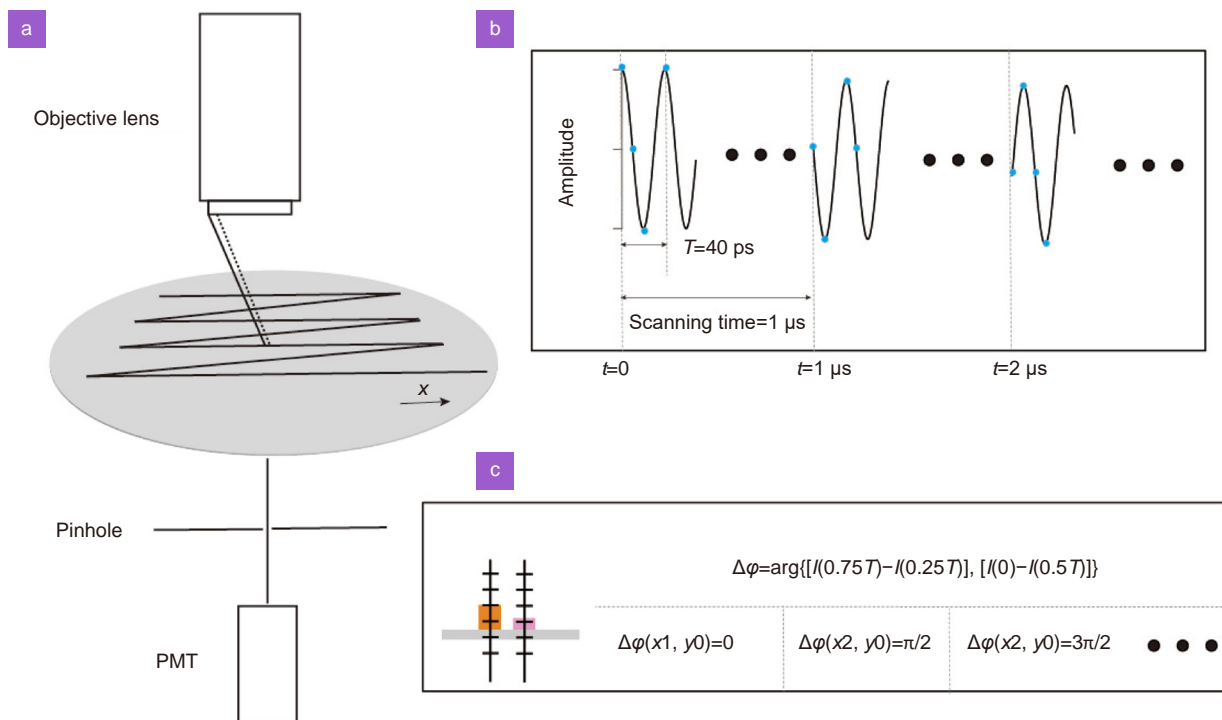

Fig. S2 | (**a**) Schematic diagram of laser-scanning image processing. (**b**) Normalized intensity curve recorded by PMT during three scanning period. (**c**) Schematic diagram of phase reconstruction during three scanning period.

Section 3: The effects of metalens size

We investigate the influence of different sizes on metalens performance. We use transmission, diffraction efficiency, and the full width at half maximum to characterize the metalens performance in this work. Here, the transmission efficiency is defined as the energy transmitted through the planar metalens to the incident energy, and the diffraction efficiency is defined as the focused light intensity to the energy transmitted through the metasurfaces. As shown in Fig. S3(a), In a certain focal length, the transmission efficiency remains almost constant as the lens size increases, while the diffraction efficiency gradually decreases from ~80% in diameters of 20 μm to ~60% after diameters ×2 processing. By contrast, the FWHM in the *x*-direction decreased from ~704 nm in diameters of 20 μm to ~508 nm after diameters ×2 processing as

shown in Fig. S3(b). It achieved the super-diffraction focusing phenomenon along *x*-direction, corresponding to the red region. Such reciprocal changes suggest that we must balance efficiency and resolution based on the actual situation. The simulation was carried out on a laptop with 12th Gen Intel(R) Core (TM) i7-12700H CPU, and each simulation used 14 cores.
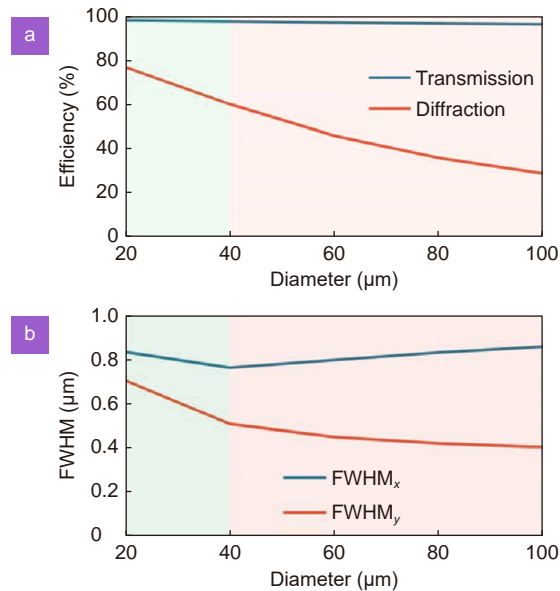

Fig. S3 | (a) Transmission and diffraction efficiencies for metalens with different lens size (focal length *f* = 10 μm). (**b**) FWHM in *x* direction and *y* direction for metalens with different lens size (focal length *f* = 10 μm).

Section 4: Robustness test

We conducted an additional simulation to further demonstrate the capability of the proposed method under a realistic optical condition. Robustness testing in phase recovery is performed to verify the stability and reliability of phase recovery algorithms when facing uncertainties, noise, or other disturbances. This type of testing aims to ensure that phase recovery algorithms can accurately restore phase information even under various complex real-world conditions. Specifically, we employed a scattering medium layer, and we increased the number of different placement positions of the PMT. In this test, we randomly selected 25 observations and averaged the measurement errors for all of them. As shown in Fig. S4, the average error in extracting phase information is about 0.2 radians even when the maximum interference phase is ~0.5π. The results showed that the proposed method was able to reconstruct high-quality images on different random positions, demonstrating the potential of our method for practical applications. The results are simulated using the angular spectrum diffraction method. Considering feasible computation time, an aperture of 200 μm (about 200λ)
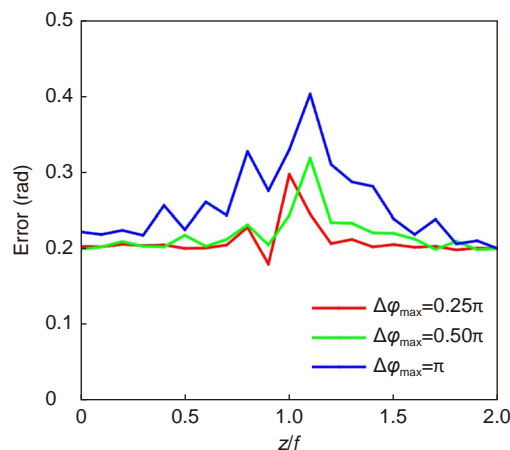

Fig. S4 | Average error for different 25 observation positions.

with 2001 sampling points (the minimal feature is 10 nm) was chosen.

Section 5: Comparisons among different optical imaging techniques

Imaging through scattering media such as biological tissues has been a challenge in optical imaging. To overcome this limitation, it has led to the development of anti-scattering techniques such as ballistic imaging and diffuse optical imaging. To further highlight the novelty and impact, we have made a comprehensive comparisons among 5 different optical imaging techniques in spatial resolution, temporal resolution, live-cell compatibility, and anti-scattering capability level. Stimulated emission depletion (STED) microscopy requires sophisticated microscopy architectures and high illumination intensities to provide sub-diffraction resolution[S1]. Problems like photobleaching and phototoxicity resulted in low temporal resolution and poor live-cell compatibility. SIM (Structured Illumination Microscopy) requires multiple exposures and complex image processing, which increases imaging time. high-contrast TIRF-SIM and GI-SIM imaging is largely limited to imaging depths of 0.1 to 1 μm[S2–S4]. The principle of confocal microscopy is based on the concept of optical conjugation and uses a pinhole aperture to achieve super-resolution imaging. However, by filtering out stray light from non-focal planes, it only has little anti-scattering capability[S5–S7]. Even for advanced commercialized microscopes (LSM 900, Zeiss) valued in the millions. It's difficult to see clear images in thick samples. Laser-scanning gradient light interference microscopy (LS-GLIM) is obtained by modifying LSM 900, and achieve confocal-level depth sectioning on unlabeled specimens. To the best of our knowledge, represent the best anti-scatter performance among any types of high resolution microscopy experimentally reported so far. However, LS technique and the serial detection of several frames in phase-shifting methods suffer from low throughput, which limits many applications that require high temporal resolution[S8]. For all the five approaches, the SWM has the evident advantage on the living cells imaging in spatial resolution, temporal resolution, system compactness, anti-scattering capability level.

As a ballistic light imaging method, SWM faces challenges and caveats often associated with the scattering mean free path ℓt, that is, the fraction of the ballistic light after traversing a scattering medium of thickness L will be given by the Lambert–Beer law: $e^{-L/\ell t}$[S9]. To reach greater depths, one must use multiple-scattered light for imaging rather than discard it. Researchers can utilize advanced imaging methods such as the wavefront shaping technique[S10] to further enhance imaging depth beyond a few scattering mean-free paths. Finally, an exciting next step is to investigate the promising applications of synthetic waves in the field of vector light, such as radially polarized light. The integration of multiple waves holds great potential in the field of optical detection and continues to be a topic of active research.

Section 6: Reconstruction phase profiles of a fresnel lens

Figure S5(a) Illustration of the entire measurement set-up, which comprises four main components: a synthetic wave source generation module, an imaging module, a custom-built microscope, and a detection module. The synthetic wave sources generation module comprises a collimated laser (with a central wavelength of 1064 nm and a power of approximately 50 W), two beam splitters (BS), an acousto-optic modulator (AOM, operating at a frequency of 80 MHz), two mirrors, an iris, and an attenuation tablet. The iris serves as a filter, eliminating zero-level energy and allowing only the first-order diffraction levels to pass through. The attenuation tablet regulates the energy of subwave 1 to ensure the energy of both subwave 1 and subwave 2 are equal. After passing through the first BS, half of subwave 1 undergoes modulation by the AOM, resulting in a frequency shift of 80 MHz, and transforming into subwave 2. Subsequently, following the iris, subwave 2 and subwave 1 recombined in the second BS to generate synthetic wave.

The imaging module consists of a lens, a sample, and a scattering medium. The scattering medium used is frosted glass (LBTEK DW110-1500), as depicted in the orange rectangular box in Fig. S5(b), and it was positioned between the lens and the sample. The sample is a diffractive optical element (DOE), specifically a Fresnel lens.

The objective lens and tube lens together form a custom built microscope, which primarily utilized for the imaging of focusing on plane, thereby enabling precise control over synthetic wave to focus accurately on the sample surface and allowing for exact adjustment of the distance between the focal spots. The DOE is placed at the focal plane of lens, which is illuminated by a synthetic wave, and is imaged using the custom built microscope. As shown in Fig. S5(c), the marking on the imaged sample, a fork symbol, is clearly seen. Furthermore, by slightly adjusting the second BS in synthetic wave source generation module, the two focal spots are separated, albeit with a non-perfectly round shape due to the
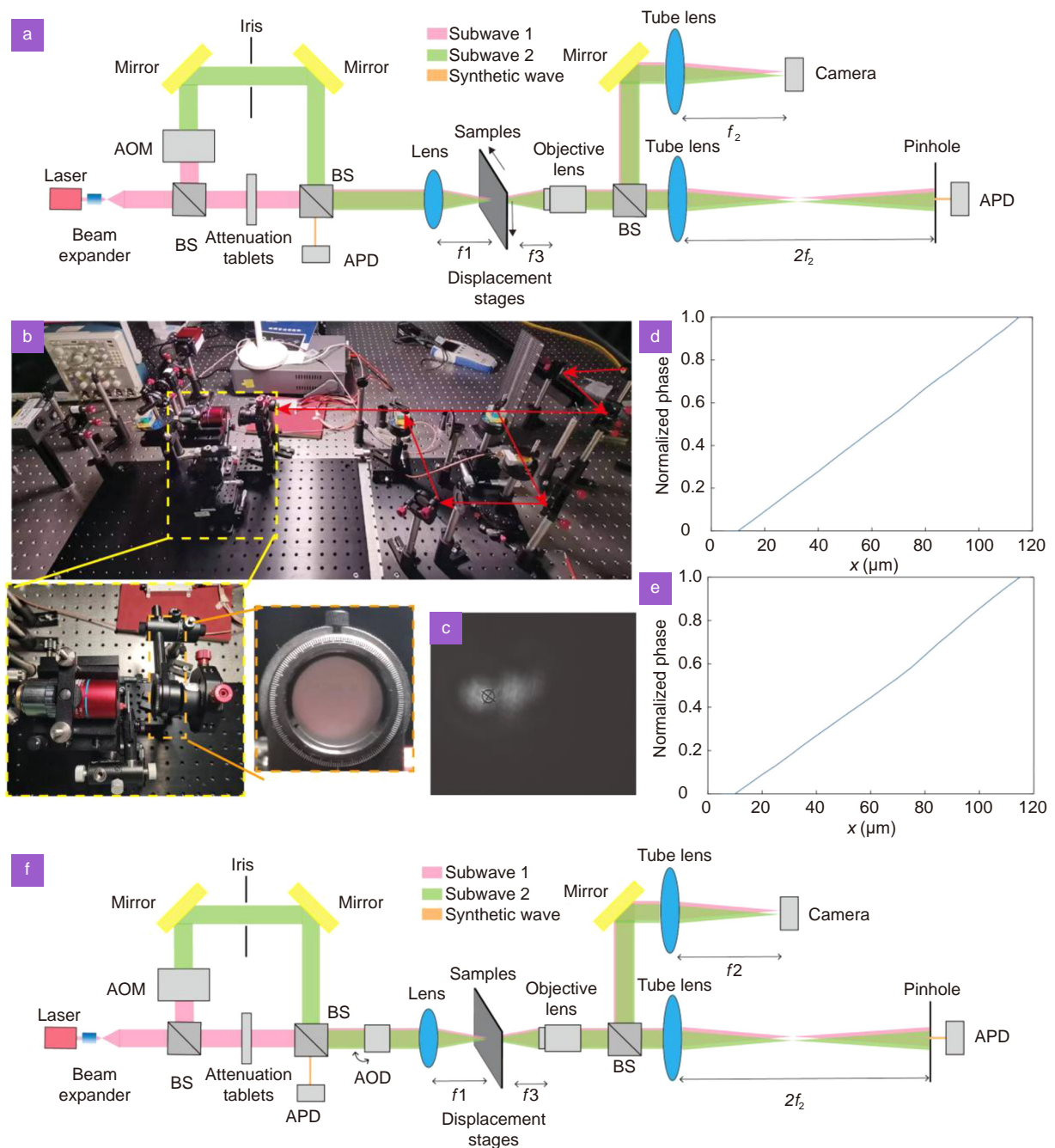
Fig. S5 | (**a**) Illustration of the entire measurement set-up. Laser (precilaser FL-SF-1064-50-cw); BS, beam splitter; APD (Thorlabs APD 310), avalanche diode photodetector; AOM (KG-AOM-1064-80M-A), acousto optic modulator. The focal lengths of the lens and tube lens are f_1 = 50 mm and f_2 = 100 mm, respectively. The working lengths of the objective lens is f_3 = 10 mm. (**b**) Layout of the entire measurement set-up. The image module is shown in the yellow rectangular box. The scatter layer is a frosted glass (LBTEK DW110-1500) shown in the orange rectangular box. (**c**) Measured images of the sample in the displacement stage with the lens. (**d**) Reconstruction phase profiles of the sample without the scattering layer. (**e**) Reconstruction phase profiles of the sample with the scattering layer. (**f**) Illustration of the future measurement set-up. AOD, acoustic-optic scanning device (OPTO-ELECTRONIC DTSXY A6).

influence of the scattering medium. Achieving two spots of the same size, with a clear separation, is crucial for imaging and represents the current experimental challenge that we are addressing in our ongoing research.

The synthetic wave signal, which is defined as light intensity variation of a virtual pinhole, is detected using APD with ps-level detection accuracy. The virtual pinhole, with a diameter of 40 μm equivalent to that of the APD's light-passing aperture, is positioned at a distance twice the focal length of the lens. It's important to note that the pinhole diameter

must be smaller than the size of the interference stripe. While a smaller pinhole can accurately reconstruct phase information, it also inevitably leads to images with low signal-to-noise ratios. Consequently, high-quality images can be produced by utilizing a properly sized hole and a point detector with enhanced detection sensitivity. The DOE is mounted on a three-dimensional translation stage (LS60-XYZ), and manual adjustments are made to its position along the x-axis. We measured 13 points at intervals of 10 μm. The ideal phase is a linearly increasing gradient phase. The reconstructed phase distribution, as illustrated in Fig. S5(d), closely approximates the ideal phase. Upon introducing this scattering medium into the optical path, as illustrated in Fig. S5(e), the reconstructed phase remains almost unchanged, which demonstrate the robust anti-scattering capability of the SWM. Figure 1(a) illustrates the simplified SWM system configuration. One of components is a synthetic wave source generation module, which uses two scanning systems. Note that, we used two scanning systems to achieve fine-tuning resolution and test imaging quality for concept validation. As depicted in Fig. S5(f), the final optimized design only uses one scanning system, which includes an AOD, specifically designed for high-speed scanning in the megahertz range.

Section 7: 2D real-time reconstruction of a neuron cell

Table S1 | Objective evaluation parameters of the different optical imaging techniques.

Method	STED[S1]	SIM[S2–S4]	Confocal[S5–S7]	LS-GLIM[S8]	SWM
Super-resolution	☺ ☺ ☺	☺ ☺ ☺	☺ ☺ ☺	☺ ☺ ☺	☺ ☺ ☺
Temporal resolution	☺	☺	☺ ☺ ☺	☺ ☺	☺ ☺ ☺
Penetration depth	☺	☺	☺	☺ ☺ ☺	☺ ☺ ☺
Live-cell compatibility	☺	☺ ☺ ☺	☺	☺ ☺ ☺	☺ ☺ ☺

As depicted in Fig. S6, the real-time phase information of a neuron cell is reconstructed. SWM allows for clear visualization of the nucleolus and the dendrites of the neuron cell. The SWM image records the dynamic changes of neuronal cells and does not suffer from scattering medium, phototoxicity, or photobleaching while maintaining a super-resolution image with high contrast.
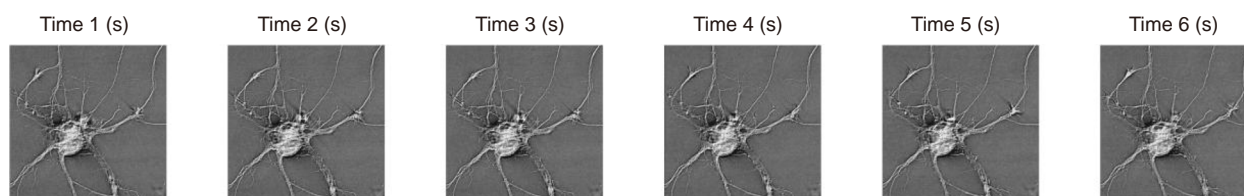
| Time 1 (s) | Time 2 (s) | Time 3 (s) | Time 4 (s) | Time 5 (s) | Time 6 (s) |

Fig. S6 | 2D real-time continuous reconstruction of a neuron cell.

References

S1.　Vicidomini G, Bianchini P, Diaspro A. STED super-resolved microscopy. *Nat Methods* **15**, 173–182 (2018).

S2.　Huang XS, Fan JC, Li LJ, Liu HS, Wu RL et al. Fast, long-term, super-resolution imaging with Hessian structured illumination microscopy. *Nat Biotechnol* **36**, 451–459 (2018).

S3.　Guo YT, Li D, Zhang SW, Yang YR, Liu JJ et al. Visualizing intracellular organelle and cytoskeletal interactions at nanoscale resolution on millisecond timescales. *Cell* **175**, 1430–1442.e17 (2018).

S4.　Li D, Shao L, Chen BC, Zhang X, Zhang MS et al. Extended-resolution structured illumination imaging of endocytic and cytoskeletal dynamics. *Science* **349**, aab3500 (2015).

S5.　Singh V R, Yang Y A, Yu H, Kamm R D, Yaqoob Z et al. Studying nucleic envelope and plasma membrane mechanics of eukaryotic cells using confocal reflectance interferometric microscopy. *Nat Commun* **10**, 3652 (2019).

S6.　Wang JF, Yang M, Yang L, Zhang Y, Yuan J et al. A confocal endoscope for cellular imaging. *Engineering* **1**, 351–360 (2015).

S7.　Huff J. The Airyscan detector from ZEISS: confocal imaging with improved signal-to-noise ratio and super-resolution. *Nat Methods* **12**, i–ii (2015).

S8.　Chen X, Kandel ME, He SH, Hu CF, Lee YJ et al. Artificial confocal microscopy for deep label-free imaging. *Nat Photonics* **17**, 250–258 (2023).

S9.　Akkermans E, Montambaux G. *Mesoscopic Physics of Electrons and Photons* (Cambridge University Press, Cambridge, 2007).

S10.　Horodynski M, Kühmayer M, Ferise C, Rotter S, Davy M. Anti-reflection structure for perfect transmission through complex media. *Nature* **607**, 281–286 (2022).